Accuracy assessment of crystal orientation indexations by EBSD

Qiwei Shi, Dominique Loisnard, Yang Li, Zhe Chen, Haowei Wang, Stéphane Roux

▶ **To cite this version:**

Qiwei Shi, Dominique Loisnard, Yang Li, Zhe Chen, Haowei Wang, et al.. Accuracy assessment of crystal orientation indexations by EBSD. Measurement Science and Technology, In press, 10.1088/1361-6501/ad204d . hal-04413357

HAL Id: hal-04413357
https://hal.science/hal-04413357v1

Submitted on 23 Jan 2024

HAL is a multi-disciplinary open access archive for the deposit and dissemination of scientific research documents, whether they are published or not. The documents may come from teaching and research institutions in France or abroad, or from public or private research centers.

L'archive ouverte pluridisciplinaire **HAL**, est destinée au dépôt et à la diffusion de documents scientifiques de niveau recherche, publiés ou non, émanant des établissements d'enseignement et de recherche français ou étrangers, des laboratoires publics ou privés.

Accuracy assessment of crystal orientation indexations by EBSD

Qiwei Shi[1,2], Dominique Loisnard[3], Yang Li[2*],
Zhe Chen[2*], Haowei Wang[2], Stéphane Roux[4]
1: SJTU-Paris Elite Institute of Technology,
Shanghai Jiao Tong University, Shanghai, 200240, China
2: School of Materials Science and Engineering,
Shanghai Jiao Tong University, Shanghai, 200240, China
3: EdF R&D, Site des Renardières, avenue des Renardières,
Ecuelles, F-77818 Moret-sur-Loing, France
4: Université Paris-Saclay, CentraleSupélec, ENS Paris-Saclay, CNRS,
LMPS - Laboratoire de Mécanique Paris-Saclay, F-91190, Gif-sur-Yvette, France
E-mail: liyang772@sjtu.edu.cn, zhe.chen@sjtu.edu.cn

January 23, 2024

Abstract

Accuracy and uncertainty analyses are essential for every measurement technology. In crystal orientation indexation by electron backscatter diffraction (EBSD), a series of accuracy estimations have been made for the Hough transform and dictionary indexation methods. The mean angular deviation is a standard parameter to indicate orientation accuracy, but this criterion is indirect and closely related to the accuracy of the projection center coordinates. Precise known orientation relationships are necessary to evaluate orientation accuracy without the ground truth. The current work uses the natural crystal twins and hardware orientation relationships to assess the orientation accuracy directly. The accuracy level for different EBSD analysis methods is compared through four experimental data sets of varying pattern definitions and noise levels. It is found that the full pattern match (FPM) algorithms improve the accuracy as compared to Hough indexation, and the gain varies greatly between 14% for fast acquisitions and 20 times for high-quality patterns. Depending on the resolution and quality of diffraction patterns, FPM results in an accuracy of crystal orientation between 0.04° and 0.9°. Comparing the two FPM variants, matching the gradients of diffraction patterns performs better in the case of high-to-median quality acquisitions while matching the pattern itself is more accurate for more noisy and low-definition patterns.

Keyword: Crystal orientation, Error analysis, Crystal twinning, High-angular-resolution EBSD, Digital image correlation.

1 Introduction

In recent decades, electron backscatter diffraction (EBSD technique) has been revealed to be a method of choice for measuring crystallographic orientation fields in scanning electron microscopes. Multiple algorithms have

been adopted to process electron backscatter patterns (EBSP) and extract crystal orientations, such as Hough transformation [1], 3D Hough transformation [2], Dictionary Indexing (DI) [3, 4], spherical indexing [5] and convolutional neural network [6]. The word 'indexing' initially means to assign Miller indices to recognizable K-bands of the pattern, yet it is increasingly used by extension for 'orientation determination' in the community. For example, both dictionary and spherical indexing provide the crystal orientation without attributing the Miller indices. In this work, the terminology 'dictionary/spherical indexing' is used as their inventors propose. The Hough-transformation method has been commercialized and used overwhelmingly in standard EBSD equipment. Though demanding in computing capacity, dictionary indexing has proven very robust in the presence of high noise level [7] and able to distinguish phases of the same Bravais lattice and different lattice constants [8]. Several post-processing algorithms have been proposed to reduce the orientation indexation noise, such as the linear adaptation of smoothing splines filter [9], or a finite element framework to reduce orientation discontinuity [10]. Those filters result in lower estimations of geometrically necessary dislocation (GND) densities and a poorer spatial resolution.

Full pattern matching (FPM) methods have also been increasingly applied to EBSPs to calibrate EBSD acquisition and to refine crystal orientations [11, 12, 13, 14, 15, 16, 17]. FPM tunes the three coordinates of the projection center (PC) and the crystal orientation to maximize the similarity between a pair of experimental and *simulated* EBSPs. The two commonly used software for dynamical EBSP simulations are ESPRIT DynamicS from Bruker Nano GmbH and EMsoft [18]. The similarity between an experimental and simulated EBSP is quantified by normalized cross correlation [12, 14], or the sum of squared EBSP differences [19]. These two criteria have been proven equivalent for large zones of interest [20]. However, only the latter can be generalized for a non-uniform noise distribution in EBSP. Different regularization methods have been proposed on PC values to limit the degrees of freedom in FPM, such as the affine transformation of EBSD scanning indices [12], projective transformation [14], or averaging the PC values by searching a global minimum for several EBSPs [16]. The precision of crystal orientation indexation by FPM varies between 0.0058-0.03° [14, 16], much lower than conventional indexation methods as the information of every pixel in EBSP is exploited.

Recently, a specific version of FPM — named Integrated Digital Image Correlation (IDIC) — to *calibrate* EBSD tests was proposed [21]. The method simultaneously provides crystal orientations and projection center coordinates and appears numerically efficient. A proper cost function, which incorporates the noise level of experimental EBSPs, is proposed to lower calibration uncertainty. The algorithm is also highly tunable, and the number of targeting parameters can be modified freely to adapt to different scenarios [22, 23]. For example, the IDIC variant based on the pattern Gradients (IDIC-G) [24] can be used to accommodate the excess-deficiency effect. Better calibration results are obtained on high-quality EBSPs.

Evaluating the accuracy and uncertainty of the measured results is vital for any measurement. The accuracy of orientation indexation directly impacts the advanced applications of EBSD, such as in the lattice tetragonality measurement [25, 26], elastic stress estimation from strain level [27, 28], crystal lattice determination [29]. The accuracy problem frequently arises in the EBSD community (see, for example, the discussion webpage [30]). Since the early development of EBSD, the uncertainty level has been assessed repetitively [31, 32, 33, 34, 35, 36, 4, 15] for different indexations: manual, Hough, dictionary, FPM, etc. The uncertainty level has been reported to be 0.2° [36], 0.5° [31] and 1° [34] for Hough indexation, and 0.03° [15] for FPM. However, most previous works focused on the *uncertainty* rather than the *accuracy* of indexation, as the true values of crystal orientation are seldom known. One exception is Si wafer samples with known cutting planes, in which case

large EBSD scans help to calibrate the EBSD setup, and thus better assess the orientation accuracy [23]. One possible solution to the absence of true crystal orientation is to estimate the accuracy of the simulated patterns [11, 4], but the conclusion needs to be validated on experimental data. Another solution is to rely on the characteristic orientation relationship between crystal twins. Such a criterion, termed 'orientation deviation', has been proposed in Ref. [37] more than 20 years ago. For unknown reasons, this clever idea has been ignored, although it offered a very valuable ground truth to evaluate the accuracy of indexed crystal orientations. The mean angular deviation (MAD) is the most commonly used to indicate orientation accuracy [38, 39]. MAD quantifies the angular deviation between the indexed Kikuchi bands in the diffraction pattern and the theoretical bands calculated from the known crystal structure. It can be calculated on each pattern, without the knowledge of the true crystal orientation. Yet, MAD is closely related to the accuracy of calibrated projection center. For example, a perfectly indexed (no error in crystal orientation) diffraction pattern would have high MAD values if wrong PC values are used in MAD calculation. Besides, MAD is not explicit enough about the orientation accuracy [40]. Evaluation of orientation accuracy by more methods, especially on samples with unknown crystal orientations, would be highly desirable.

The present paper uses two methods to assess orientation accuracy of different EBSD indexation methods. The first relies on the special orientation relationship inside the sample, while the second generates its orientation relationship by sample rotation. The accuracy of different indexation algorithms is extensively studied on different experimental EBSD data sets. Section 2 briefly recalls the basic principles of IDIC EBSD indexation including its common tactics and the dictionary indexation methods. Section 3 evaluates orientation accuracy and uncertainty of samples containing twinning structures by IDIC EBSD. Section 4 details the method of applying physical rotations. Compared with the conventional Hough results, implementing FPM, such as IDIC EBSD indexation and dictionary indexing with refinement, significantly enhances the accuracy of crystal orientation.

2 Analysed indexation methods and adopted parameters

2.1 Summary of IDIC EBSD indexation method

A detailed explanation of the IDIC EBSD indexation method was provided in Ref. [21]. The essential notions used in the process are briefly recalled here.

The EBSD projection geometry used in the IDIC EBSD indexation is shown in figure 1 together with the two reference systems used in the paper. The coordinate system (x, y, z) is associated with the EBSP detector and (X, Y, Z) with the stage holder. The projection center (x^*, y^*, z^*) of an EBSP is defined as the coordinates of the electron beam interaction volume with respect to the EBSP detector, as illustrated in figure 1. The sample tilt angle, represented by θ in figure 1, is generally set to 70°. The sample rotation angle relative to the stage holder, denoted by β in figure 1, is generally 0°. Varying of β and θ generates a controlled overall rotation and will be discussed in Section 4.

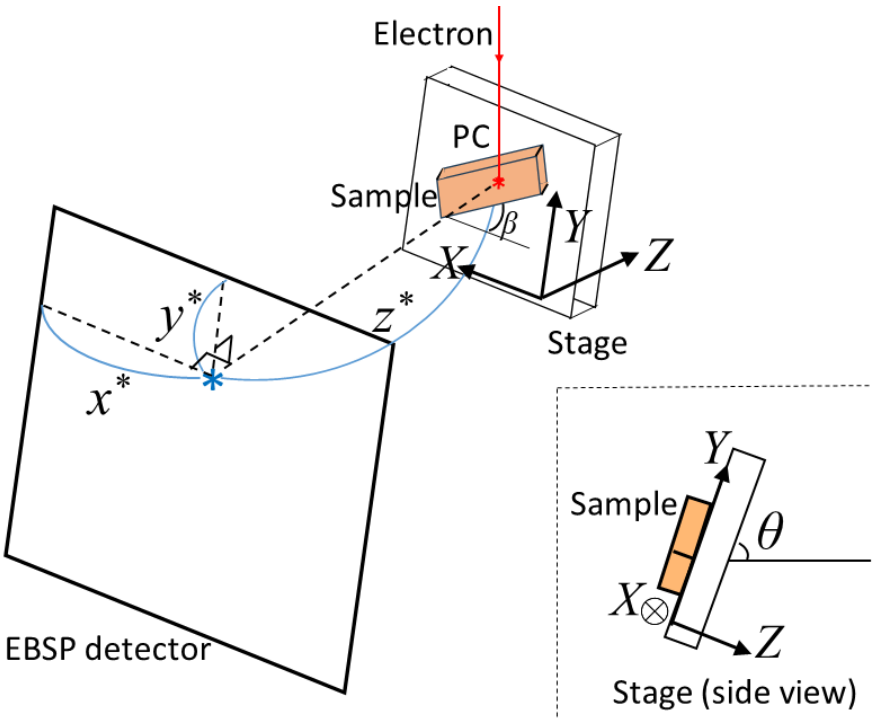

Figure 1: Geometry setup for the EBSD indexation. θ stands for the sample tilt angle, and β is the sample rotation angle with respect to the stage holder.

IDIC EBSD algorithm aims at calibrating the main projection parameters $\boldsymbol{P}$, which is a vector of 6 components consisting of the crystal orientation, noted for example by Euler angles $(\varphi_1, \phi, \varphi_2)$, and the projection center coordinates (x^*, y^*, z^*). IDIC EBSD retrieves $\boldsymbol{P}$ by correlating an experimental EBSP, noted as $f(\boldsymbol{x})$, with a simulated EBSD pattern $g(\boldsymbol{x})$. $g(\boldsymbol{x})$ is projected from the EMsoft [18] simulated master pattern $G(u, v)$ by the relation

$$g(\boldsymbol{x}) = G(\boldsymbol{u}(\boldsymbol{P}, \boldsymbol{x})) \tag{1}$$

with the stereographic projection $\boldsymbol{u}(\boldsymbol{P}, \boldsymbol{x})$ detailed in Ref [21]. Two variants have been introduced. The first one is based on the least-squares difference in the pattern itself

$$\Theta = \sum_{ROI} w(\boldsymbol{x})^2 \left(f(\boldsymbol{x}) - g(\boldsymbol{x})\right)^2 \tag{2}$$

whereas the second exploits the least-squares difference of the pattern gradients

$$\Theta' = \sum_{ROI} w(\boldsymbol{x})^2 \left[\left(f_{,x}(\boldsymbol{x}) - g_{,x}(\boldsymbol{x})\right)^2 + \left(f_{,y}(\boldsymbol{x}) - g_{,y}(\boldsymbol{x})\right)^2\right] \tag{3}$$

where $(g_{,x}(\boldsymbol{x}), g_{,y}(\boldsymbol{x}))$ is the gradient of $g(\boldsymbol{x})$, and $w(\boldsymbol{x})$ is a weight associated to each pixel, introduced to account for different noise levels observed at different pixel locations $\boldsymbol{x}$. w is set as the inverse of the uncertainty of residual fields at each pixel for different crystal orientations [21].

Both IDIC and IDIC-G indexations may be used to determine either all 6 projection parameters (3 crystal orientations and three coordinates of the projection center), $(\varphi_1, \phi, \varphi_2, x^*, y^*, z^*)$, or only the three crystal orientation components $(\varphi_1, \phi, \varphi_2)$. These two options are referred to by adding the number of parameters, 3 or 6, to the two variants IDIC or IDIC-G. After fitting to a plane, the pattern center (x^*, y^*, z^*) calibrated by IDIC6 or IDIC-G6 is imposed — and no longer modified — for the IDIC3 and IDIC-G3 based orientation

determination [21]. The iterative Gauss-Newton algorithm is used in optimizing the two cost functions, and the detailed formulas are provided in Ref. [21, 24] respectively.

2.2 Dictionary indexing

DI is an open-source EBSD indexation method incorporated in EMsoft [18]. DI creates a vast 'dictionary' of simulated EBSPs by projecting the master pattern $G(u, v)$ with a grid of projection parameters $(\varphi_1, \phi, \varphi_2, x^*, y^*, z^*)$. An experimental EBSP is matched to each item of the dictionary, and the item with the maximal inner product reveals the crystal orientation of the target pattern. Crystal orientation refinement [11, 41] can then be applied to fine tune DI results. A detailed tutorial of DI, together with several experimental datasets, is provided by Jackson*et al.* [41].

Inspired by the aforementioned DI tutorial, the following DI parameters are adopted in the present study. The same master pattern is used for both IDIC and DI, and the PC coordinates calibrated by IDIC EBSD are used in dictionary indexation in order to provide a fair comparison. The ncubochoric parameter is set to 100 to generate sufficiently dense orientation dictionary items. Masks for EBSPs are used in DI where necessary. The high pass filter width is set to 0.125, and regions for adaptive histogram equalization set to 4 as suggested in Ref. [41]. Crystal orientation refinement based on the method 'bound optimization by quadratic approximation' [11] is performed after running the initial DI.

3 Full exploitation of twin orientation relationships

A specific orientation relation (OR) is well-known to hold at twin boundaries. A precise 60°-rotation around the $\langle 111 \rangle$ crystal direction is present across twin boundaries for unstrained FCC crystalline samples. Early studies of the EBSD technique have demonstrated the difficulty of determining the rotation axis, especially for small misorientation levels [33, 42]. The twinning structure has the advantage of large misorientation. Thus it is a good candidate for judging the orientation accuracy.

Twins are easily recognizable structures in many metals. In EBSD software suites, twins are identified due to their characteristic misorientation with neighbors and twinning plane along specific directions [37]. The term 'misorientation deviation' is used in Ref. [37] to quantify the difference between the theoretical and indexed misorientation across twin boundaries. However, the mathematical formula of misorientation deviation is not expressed explicitly in [37]. Here the 'misorientation deviation' criterion is used again to evaluate the orientation accuracy based on the twinning relationship, which considers both the rotation angle and the rotation axis.

3.1 Quaternion-based accuracy evaluation algorithm for twins

Quaternion is a convenient tool to represent crystal orientations. It encodes the orientation and misorientation (rotation) easily [43]. In the convention adopted here, the first quaternion component is the cosine of half the misorientation, and the remaining three components give the rotation axis direction.

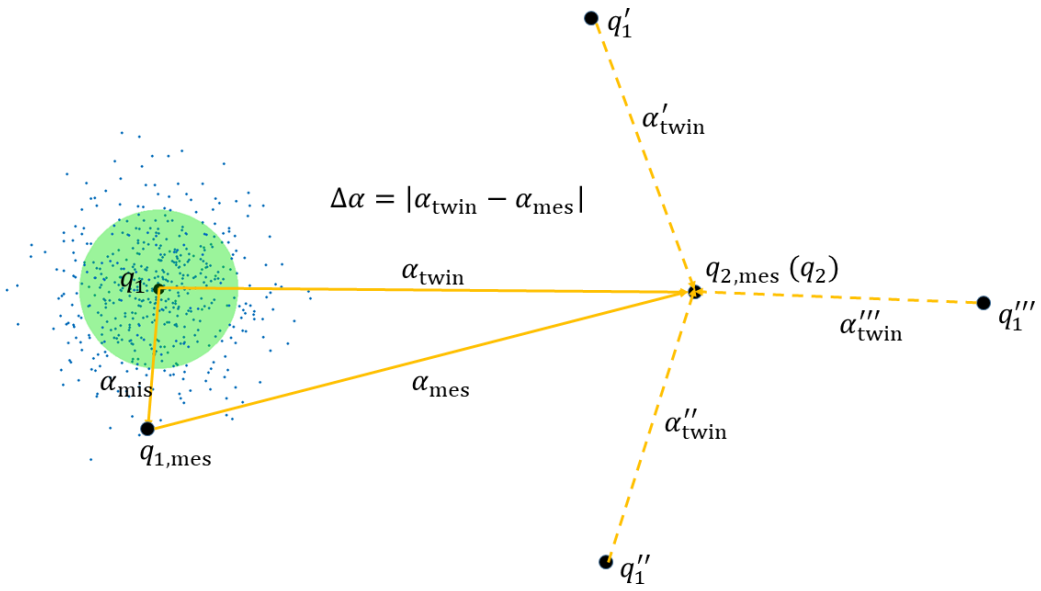

Figure 2: Sketch of the orientation accuracy metrics α_{mis} and $\Delta\alpha$ for twin boundaries.

Figure 2 is a schematic (not proportional to the actual distance) diagram of the orientation accuracy metrics at twin boundaries. $q_{1,\text{mes}}$ and $q_{2,\text{mes}}$ are the indexed crystal orientations of an EBSP pair across the twin boundary. Without loss of generality, the indexation errors of the two orientations are ascribed to $q_{1,\text{mes}}$, and $q_{2,\text{mes}}$ is assumed equal to the ground truth, noted at this moment as q_2. The misorientation deviation α_{mis} corresponds to the misorientation between the measured orientation $q_{1,\text{mes}}$ and the theoretical orientation q_1, deduced from q_2. The misorientation between q_1 and q_2 is α_{twin}, which is 60° for unstrained FCC samples. The measured misorientation at twin boundaries between $q_{1,\text{mes}}$ and q_2 is denoted α_{mes}. α_{mis} stands for the distance between the true value and the measured one; thus, it is a relevant metric of the orientation indexation *accuracy*.

To account for the misorientation angle-axis, unitary quaternions corresponding to the theoretical twinning relationship are compared to the crystal orientation pair across twin boundaries. The rotation quaternion between $q_{1,\text{mes}}$ and q_2 is defined as $q_{1,\text{mes-2}} = q_{1,\text{mes}}^{-1} * q_2$, where '$*$' stands for the quaternion multiplication, and q^{-1} means the inverse of q (equivalent to its conjugate). The theoretical rotation quaternions of FCC twins are

$$q_{\text{twin}} = \frac{1}{2\sqrt{3}} \begin{cases} [3,1,1,1] \\ [3,-1,1,1] \\ [3,1,-1,1] \\ [3,1,1,-1] \end{cases} \tag{4}$$

The misorientation deviation quaternion is defined as the distance between $q_{1,\text{mes-2}}$ and q_{twin}:

$$q_{\text{mis}} = q_{1,\text{mes-2}}^{-1} * q_{\text{twin}} \tag{5}$$

The misorientation deviation α_{mis} — a scalar value indicating the distance of experimental and theoretical twin orientation relationship — is defined as

$$\alpha_{\text{mis}} = 2\arccos\left(q_{\text{mis}}(1)\right) \tag{6}$$

where $q_{\text{mis}}(1)$ denotes the first component of the quaternion q_{mis}.

Note that α_{mis} is chosen as the minimum of the 4 q_{twin} variants are adopted, as the twinning could be along any q_{twin}. For example, the four unitary quaternions corresponding to the twinning generate four candidate quaternions based on q_2, as noted by q_1, q_1', q_1'', q_1''' in Figure 2. q_1 is retained among the four candidates as it is the closest to the measured one $q_{1,\text{mes}}$.

Another possible metric for the distance to twinning orientation relationship is $\Delta\alpha$, which is named 'misorientation difference' and defined as

$$\Delta\alpha = |\alpha_{\text{mes}} - \alpha_{\text{twin}}| = |2\arccos\left(q_{1,\text{mes-2}}(1)\right) - \alpha_{\text{twin}}| \tag{7}$$

α_{mis} exploits the misorientation angle-axis of the twin orientation relationship, while $\Delta\alpha$ only considers the misorientation angle. Naturally, $\Delta\alpha$ underestimates the orientation indexation error. In figure 2, the green sphere around q_1 highlights the median value of α_{mis}, larger than the median value of $\Delta\alpha$.

It is interesting to compare both accuracy metrics, misorientation deviation α_{mis} and misorientation difference $\Delta\alpha$. Figure 3a compares the distributions of α_{mis} and $\Delta\alpha$ for the nickel data set A explained in Section 3.2, considering EBSPs at twin boundaries indexed by IDIC-G3. The same curves for 5000 randomly generated crystal orientations at twin boundaries are shown in Figure 3b. To generate these virtual data, a pair of unit quaternions q_1, q_2 of exact FCC twin orientation is created, then 5000 Rodrigues' vectors ω_{rand} whose three components are all normally distributed are generated. Theoretically, a pure random error of orientation determination suits the spherical normal distribution [36], which reduces to normal distribution for small misorientations. The parameters of the normal distribution are 0 for the mean, and 0.0035 rad (equals to 0.2°) for the standard deviation. The random Rodrigues' vectors are transformed into unitary quaternions:

$$q_{\text{rand}} = \left[\sqrt{1 - |\omega_{\text{rand}}|^2}, \omega_{\text{rand}}\right]$$

Then the 5000 q_{rand} are multiplied to q_1 to get 5000 $q_{1,\text{rand}}$. The orientations $q_{1,\text{rand}}$ and q_2 are counterparts for the experimental data at twin boundaries and are then analyzed to provide theoretical references of α_{mis} and $\Delta\alpha$. The shapes of α_{mis} and $\Delta\alpha$ for both experimental and virtual data are comparable, except for the long tail to the right for the experimental data. Note that although the log-normal law is often chosen to fit orientation indexation errors for experimental results [44, 40], it is merely a descriptive representation of the measured orientation inconsistency, including the true misorientation due to microscopic strains and the false one due to deteriorated pattern quality. The distribution of $\Delta\alpha$ shows that it consistently underestimates the orientation indexation error for experimental and randomly generated orientations, as the rotation axis information is not considered. Another key difference between the two curves is at the 0°: almost no indexation point has 0° of misorientation deviation, yet the misorientation difference is maximum at 0°.

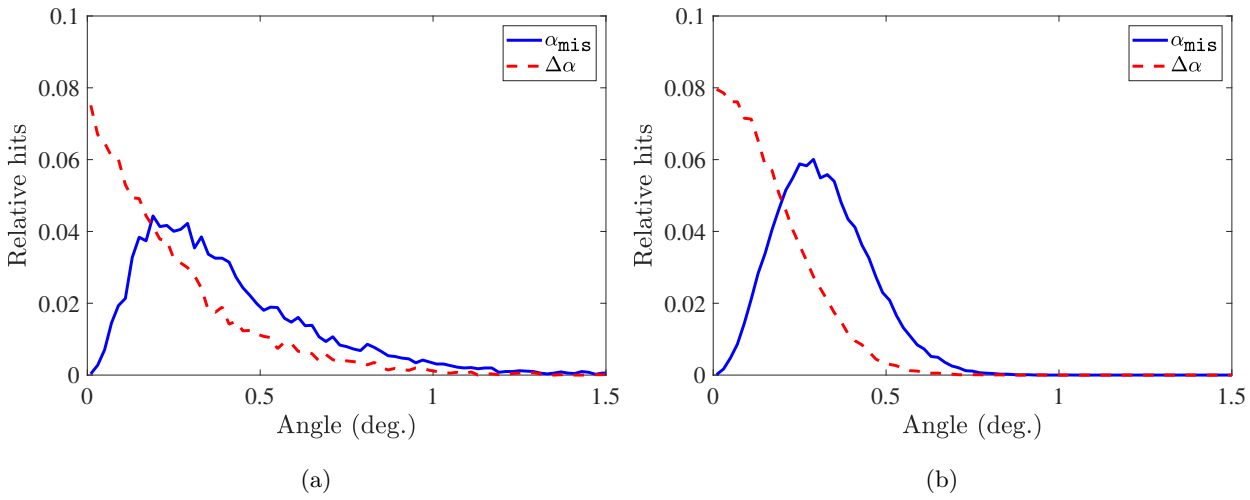

Figure 3: Comparison of distributions of misorientation deviation (α_{mis}) and misorientation difference ($\Delta\alpha$) at twin boundaries for (a) dataset A explained in Section 3.2 and (b) randomly generated orientations.

As a result, the misorientation deviation α_{mis} will be used to evaluate orientation accuracy of twins in the following section 3.2.

3.2 Examples of accuracy evaluation for twins

Two EBSD data sets of two commercial Ni samples are used to characterize the accuracy of EBSD analysis methods. No strain is introduced in both samples. Thus the local misorientation is expected to be negligible.

A data set is acquired by the Bruker e$^-$Flash^{HD} EBSD detector mounted on a Tescan MIRA3 scanning electron microscope. The acceleration voltage is 20 kV, the beam current is 10 nA, and the step size is 0.61 µm. A total of 67500 median-resolution (228×320 pixels) diffraction patterns are recorded, covering an area of 137×183 µm^2. This medium-quality data set is referred to as A. The indexation methods IDIC-G6&3, IDIC6&3, DI with and without refinement, and Hough transform are all tested on this data set.

Another data set (B) acquired by an EDAX Hikari Super Camera is provided by Wright *et al.* [45] and shared by Jackson *et al.* [41]. The resolution of each EBSP is small 60×60 pixels, the dwelling time 8 ms and the step size 1.5 µm. This data set is representative of fast-acquisition pattern qualities with a high noise level. The Hough indexation and dictionary indexation (with or without refinement) results are shared by Jackson *et al.* [41], and the indexation by IDIC6 and IDIC3 are all analyzed here to estimate their accuracy levels.

An EBSP of data set A is shown in Figure 4a. The orientation map shown in Figure 4b contains numerous twins, where the black dots highlight the pixels at twin boundaries used for accuracy estimation. Figures 4c–4f show the kernel average misorientation (KAM) maps calculated with IDIC-EBSD, Hough indexing, DI with and without refinement, respectively. KAM values based on the four closest neighbors indicate the orientation uncertainty for this unstrained sample. The KAM field by IDIC3 and refined DI are much lower than the Hough indexation, and several scratches on the sample surface during preparations are apparent. KAM of DI without refinement only highlights the grain boundaries, and is insensitive to the orientation oscillations below its orientation grid step, as shown in Figure 4e.

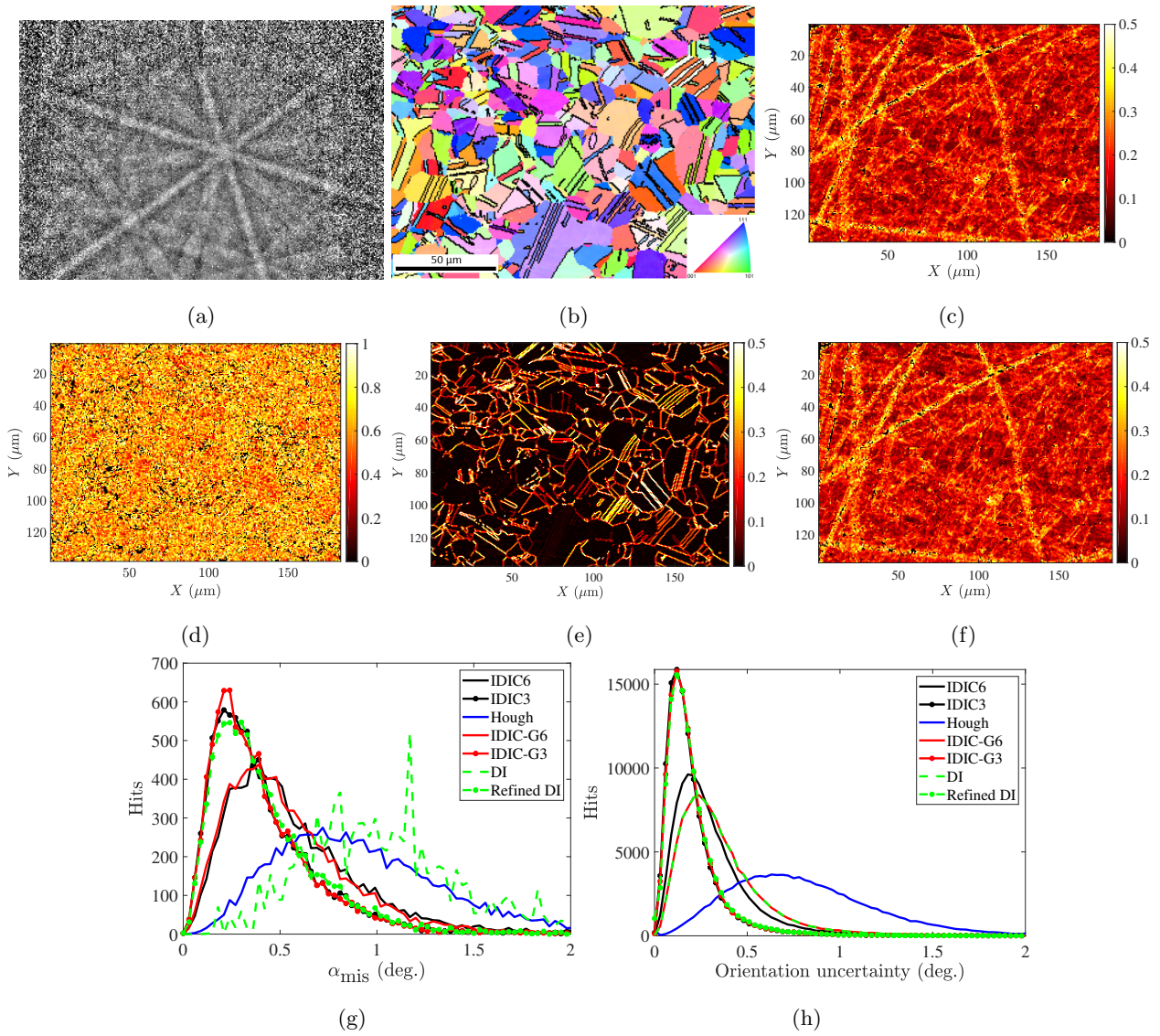

Figure 4: (a) A raw EBSP of resolution 228×320 of a Ni alloy, data set A; (b) Corresponding inverse pole figure-Z map; (c) Kernel Average Misorientation (KAM) map calculated by IDIC3; (d) KAM map by Hough indexation provided by Bruker; (e) KAM map by dictionary indexation; (f) KAM map by DI with refinement; (g) The misorientation deviation distribution for pixels at twin boundaries. (h) The uncertainty (precision) distribution of orientation indexation, represented by the KAM field. The results of several different indexation methods are compared.

Figure 4g plots the histograms of misorientation deviation obtained with different indexation methods, while Figure 4h plots the corresponding histograms of KAM values. Though the uncertainty level is higher for IDIC-G6 than IDIC6, IDIC-G6&3 achieves slightly better accuracy, *i.e.,* smaller α_{mis}, than IDIC6&3 (the exact values will be shown in Table 1). These results demonstrate that for median-resolution EBSPs, IDIC-G enhances the accuracy yet increases the uncertainty of crystal orientation indexation compared to IDIC [24]. Besides, the refined DI and all versions of IDIC-G and IDIC outperform Hough indexation.

An exemplary EBSP for data set B is shown in Figure 5a. The orientation map shown in Figure 5b contains numerous twins, where the black dots highlight again the pixels at twin boundaries used for accuracy estimation. Figures 5c-5f show the KAM maps calculated with IDIC3, Hough indexation, and dictionary indexing before

and after refinement, respectively. The Hough KAM field averages around 0.600°, while IDIC3 leads to a KAM field average of 0.306°. The DI KAM shows fake bright curvy features due to the discontinuous nature of the algorithm. This orientation discontinuity is effectively solved by the orientation refinement proposed by [11] as shown in Figure 5f, leading to an average KAM value of 0.317°. Figure 5g shows the histograms of α_{mis} for each algorithm. IDIC3 has the best accuracy level, followed by Hough indexation, while IDIC6 and DI without refinement have high and comparable error levels. The precision profiles of various EBSD analysis methods, evaluated as the KAM values, are compared in Figure 5h. The KAM value of dictionary indexing without refinement reduces to several distinct intervals, with most KAM at 0°. Again, IDIC3 outperforms Hough and IDIC6 in terms of indexation uncertainty.

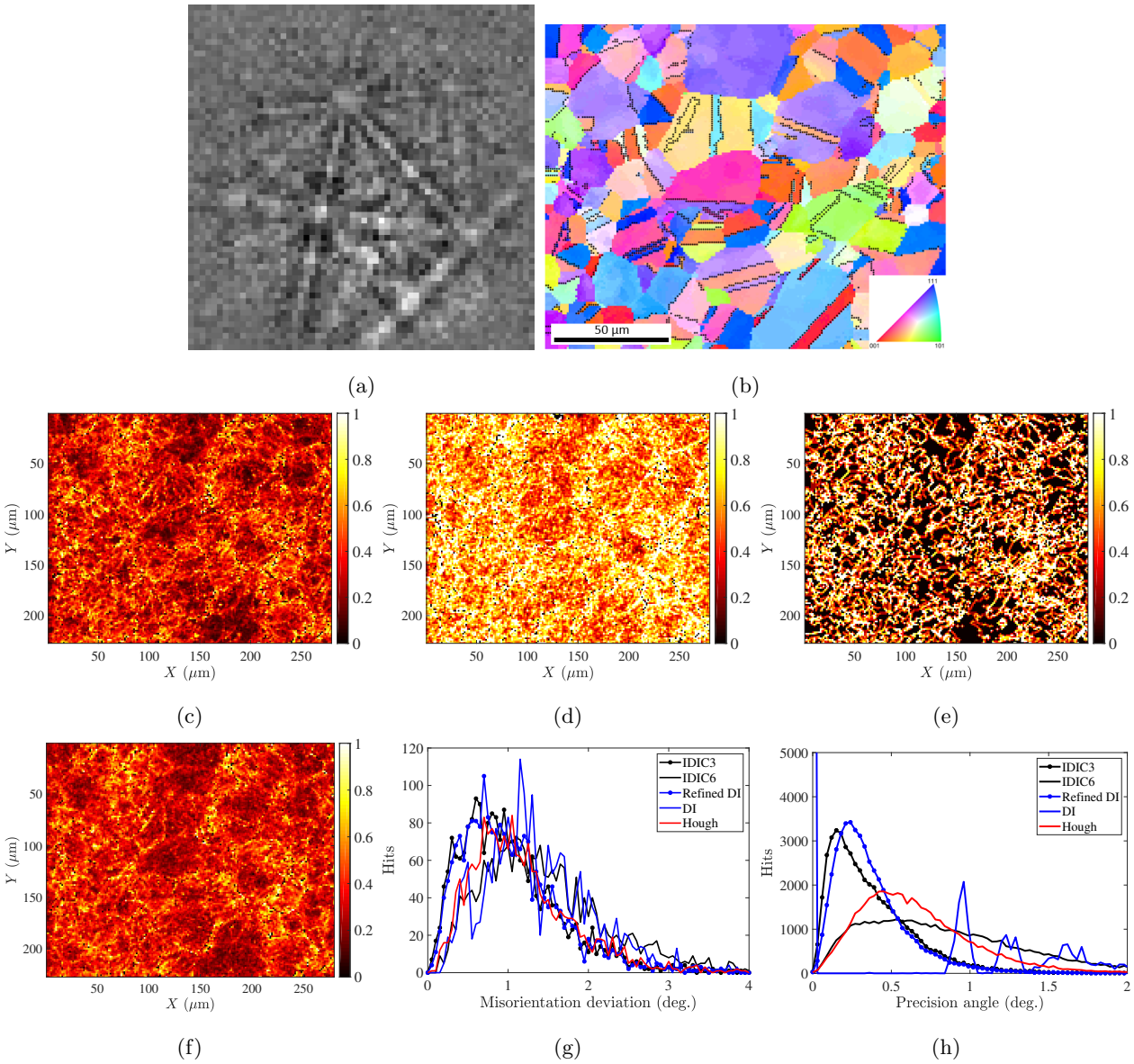

Figure 5: (a) A raw EBSP of resolution 60×60 of a Ni alloy, data set B. (b) The inverse pole figure-Z of the Ni sample. Black dots mark the pixels at twin boundaries; (c) Kernel average misorientation map computed with IDIC3; (d) KAM map with Hough indexation provided by Bruker; (e) KAM map with dictionary indexation provided by Jackson *et al.* [41]; (f) KAM map with refined dictionary indexation provided by Jackson *et al.* [41]; (g) The misorientation deviation distribution for pixels at twin boundaries; (h) The KAM distribution. The results of several different indexation methods are compared.

To sum up, this section proposes to evaluate the orientation accuracy by fully exploiting the twinning orientation relationship, including the misorientation angle and the rotation axis. The misorientation deviation α_{mis} better indicates the orientation accuracy than the misorientation difference $\Delta\alpha$. Depending on the resolution of EBSPs, IDIC-G3/IDIC3 outperforms the DI and Hough transform, while the refined DI achieves similar accuracy to IDIC-G3/IDIC3. More statistics are summarized in Table 1.

4 Multiple acquisitions with controlled rotations

Apart from the natural crystal orientation relationships such as twins, multiple EBSD acquisitions of the same sample area with controlled rotations can also reveal the EBSD accuracy. Here the sample tilt angle θ and rotation angle β around the sample normal are analyzed to assess its feasibility.

4.1 Acquisitions with different tilt angles θ

The optimal experimental setup of EBSD acquisition corresponds to the maximal backscatter electron generations. Usually, it implies a 70°-tilted sample with the projection center lying in the upper region of the detector. Yet many previous works have adopted specific experimental setups to study different phenomena. Different rotations were applied on a series of EBSPs, or around the sample surface normal, to probe the rotation axis imprecision when the rotation angle is small [33, 42]. Winkelmann *et al.* have adopted smaller tilt angles to study the electron absorption and gray level reversal [46]. In our previous work [21], the same area on a polycrystalline Al-Mg alloy sample was scanned with different tilt angles θ to study the consistency of orientation indexation. This method of accuracy evaluation is further explored here below.

An Al-Mg sample is mechanically polished and chemically etched to prepare for the EBSD acquisition. High definition (1200× 1600 pixels) diffraction patterns recorded by Bruker e$^-Flash^{HD}$ EBSD detector are analyzed to provide a 30×40 map of crystalline orientation, resolved at a step size of 3.43 µm. The acceleration voltage is 20 kV, the probe current 20 nA, and the dwell time 0.9 s. A series of EBSP is acquired with different sample tilt angles (70°, 65° and 60°) on the same sample area to demonstrate the performance of the indexation algorithms on different tilt angles. This data set is denoted C in the following. Note that it has been used in our previous works for different purposes [21, 24].

Figures 6a-6c show the EBSPs of the same sample point while tilted at 70°, 65°, and 60° respectively. Lines mark the band positions changing with the tilt angle. Besides, the pattern quality deteriorates as the tilt angle deviates from 70°. The gray level reversal is observed for the lower part of the pattern at 60°, as reported and successfully simulated by Winkelmann *et al.* [46]. The orientation map of the 5-grain indexed region is shown in Figure 6d.

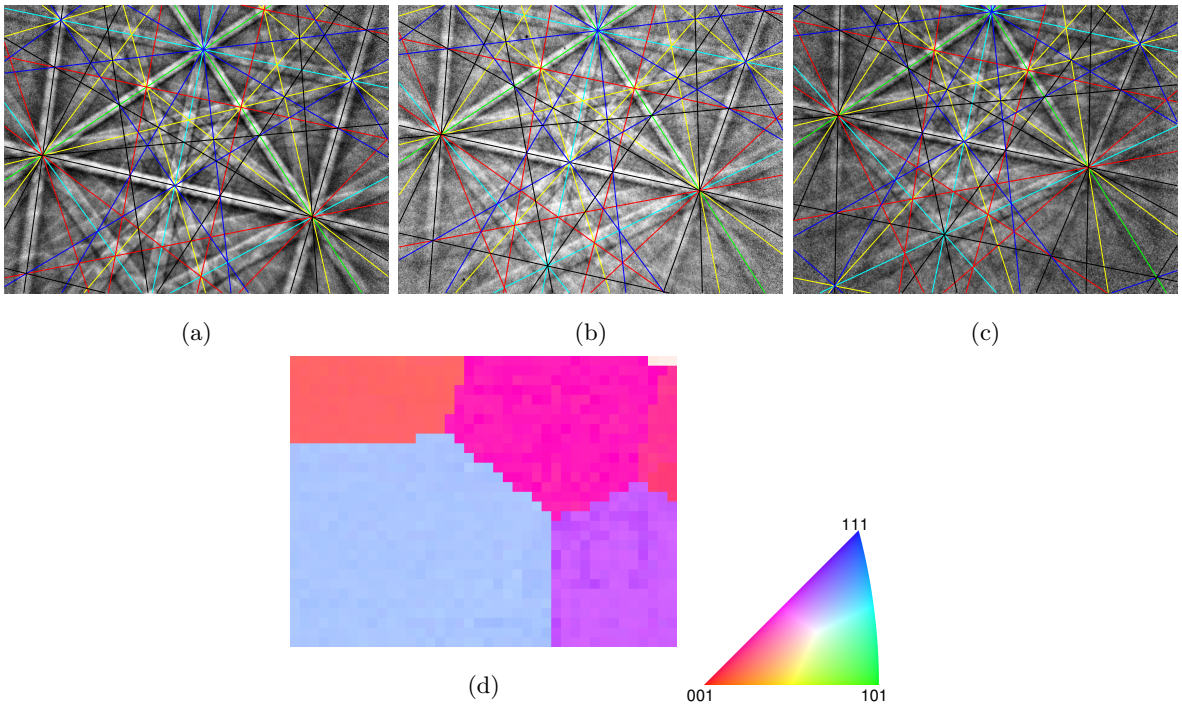

Figure 6: (a-c) EBSP of a polycrystal Al-Mg alloy (sample C) at the same position with sample tilt 70°, 65° and 60° respectively; (d) Inverse pole figure-Z of the sample.

Figure 7 shows the Rodrigues' vectors between the IDIC-G-indexed results with different sample tilt angles. The component ω_X is the most significant, while ω_Y and ω_Z are close to 0, except for the lower left grain between 65° and 60°. This indexation result is as anticipated since different tilt angles correspond to a rotation of the sample about the X direction. The indexation result is less accurate for tilt angles 60° and 65°; thus, the calculated Rodrigues' vector for this rotation is less precise.

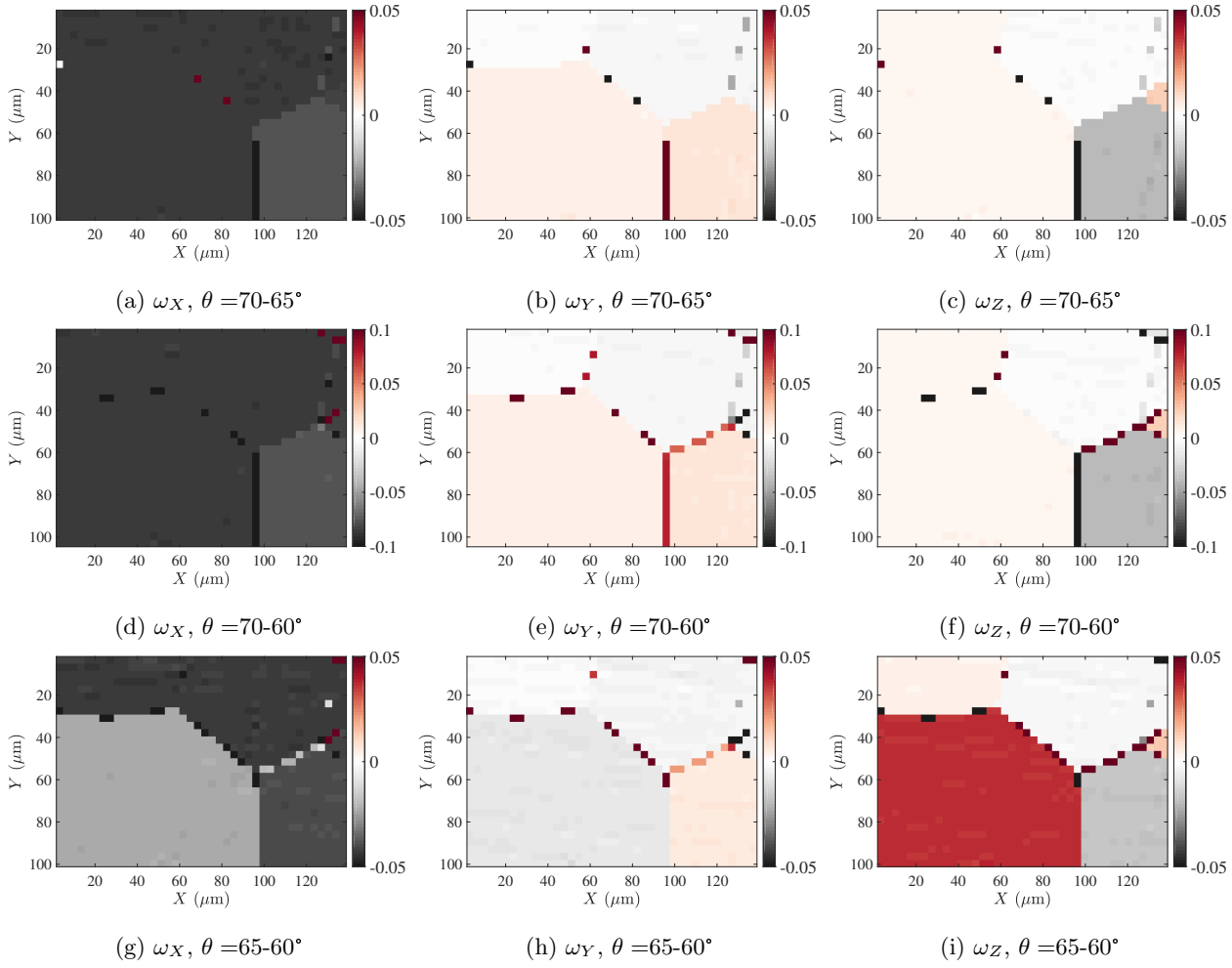

(a) ω_X, θ =70-65° (b) ω_Y, θ =70-65° (c) ω_Z, θ =70-65°

(d) ω_X, θ =70-60° (e) ω_Y, θ =70-60° (f) ω_Z, θ =70-60°

(g) ω_X, θ =65-60° (h) ω_Y, θ =65-60° (i) ω_Z, θ =65-60°

Figure 7: The Rodrigues' vector components ω_X, ω_Y and ω_Z for sample C at different tilt angles 70°, 65°, and 60°. The calculation is based on the IDIC-G3 indexation results.

Quite similar to the misorientation deviation α_{mis} defined in Section 3, α_{mis} can also be employed to evaluate the orientation accuracy in data sets with controlled rotation. The only difference is to change the unitary twinning quaternion q_{twin} to the unitary quaternion q_{rot} corresponding to the controlled rotation. The angle α_{mis} quantifies the distance between the indexed overall rotation and the applied one at different tilt angles θ. The α_{mis} fields based on Hough indexation, IDIC3, and IDIC-G3 are shown in Figure 8. The misorientation deviation with Hough indexation is around 1°, roughly three times higher than IDIC and IDIC-G methods. The α_{mis} estimated by IDIC-G EBSD calibration is closer to zero. It has been shown that IDIC-G enhances the PC calibration accuracy, thanks to its least sensitivity to the excess-deficit effect of the Kikuchi bands [24]. As the crystal orientation and PC components are closely correlated in EBSD calibration [16], IDIC-G is also expected to improve the orientation indexation. This misorientation deviation analysis based on multiple acquisitions of different tilt angles demonstrates the improved accuracy of IDIC-G EBSD indexation, significantly when the tilt angle deviates from the ideal 70°.

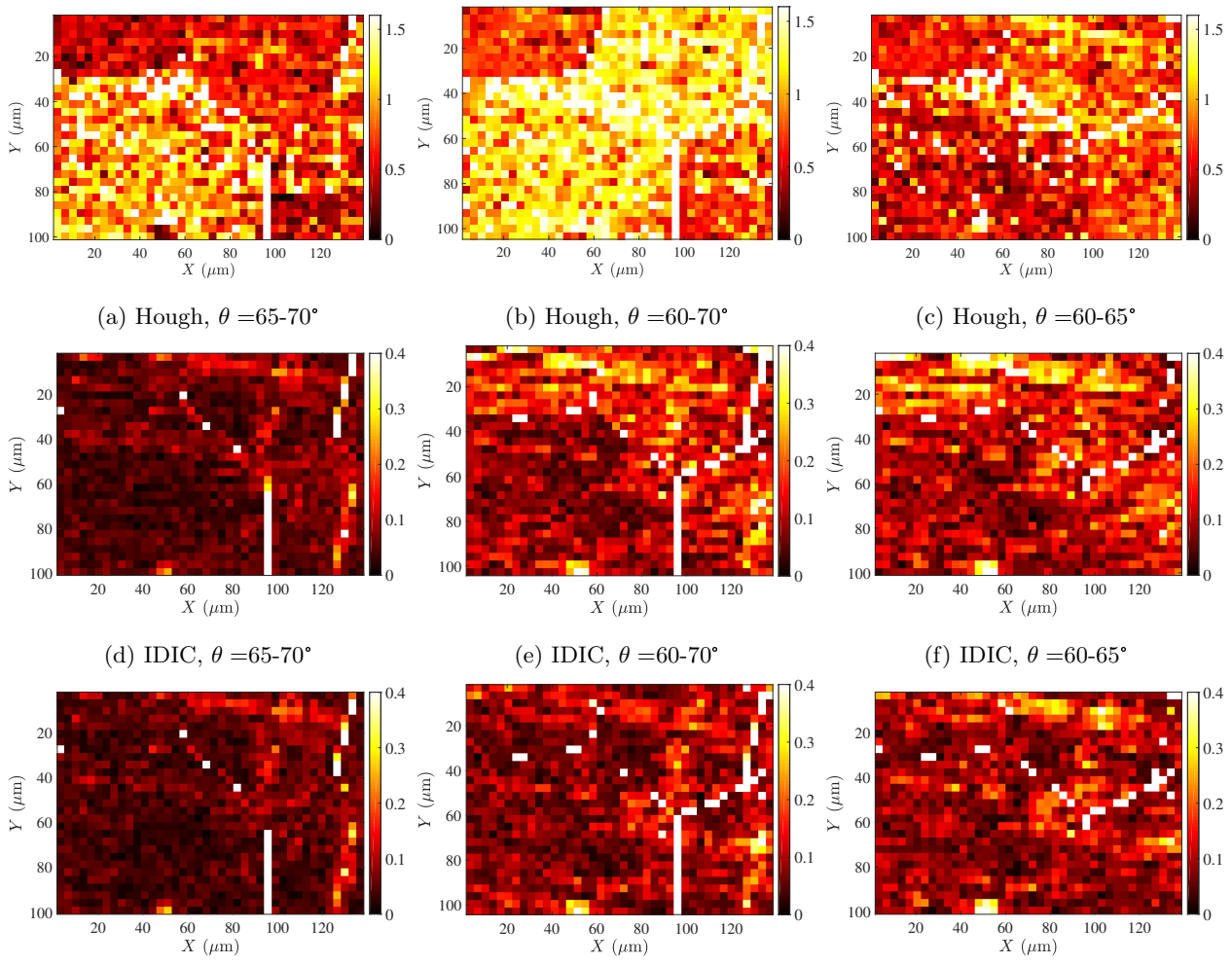

(a) Hough, θ =65-70°

(b) Hough, θ =60-70°

(c) Hough, θ =60-65°

(d) IDIC, θ =65-70°

(e) IDIC, θ =60-70°

(f) IDIC, θ =60-65°

(g) IDIC-G, θ =65-70°

(h) IDIC-G, θ =60-70°

(i) IDIC-G, θ =60-65°

Figure 8: Misorientation deviation in ° between EBSD acquisitions of sample tilt 60°, 65° and 70°, indexed by Hough transform, IDIC3 and IDIC-G3.

4.2 Acquisitions with different rotation angles β

Modifying the sample rotation angle β with respect to the stage holder is another overall rotation method. The EBSD data sets (D) of a fine-grained Zircaloy-4 shared by Birch & Britton [47] are now analyzed. The EBSD settings are as follows: magnification 1500×, step size of 1 µm, EBSP definition of 160×120, map definition of 285×191 pixels, and Bruker nano EBSD detector. Three EBSD maps covering roughly the same area are recorded, each rotated by β =0°, 50°, and 90°.

The orientation maps of the 3 acquisitions are shown in figures 9a-9c. The IPFs of β = 50° and 90° are transformed into the β = 0° frame by correlating the grain boundaries [48]. The crystal orientation remains unchanged in this process, so the grains in figures 9a-9c are at the same position, but the crystal IPFs are slightly different. The EBSPs from the three scans, of the same grain marked by the star in figure 9a, are shown in figure 9d-9f. The rotations of β are visible by comparing the 3 EBSPs. As discussed in Ref. [24], IDIC-G is not suited to low-resolution EBSPs since — without considering the correlations in the pattern noise — the method appears sensitive to a higher noise amplitude. As a result, only the indexation algorithms IDIC6 and IDIC3 are applied to the Zr data set D.

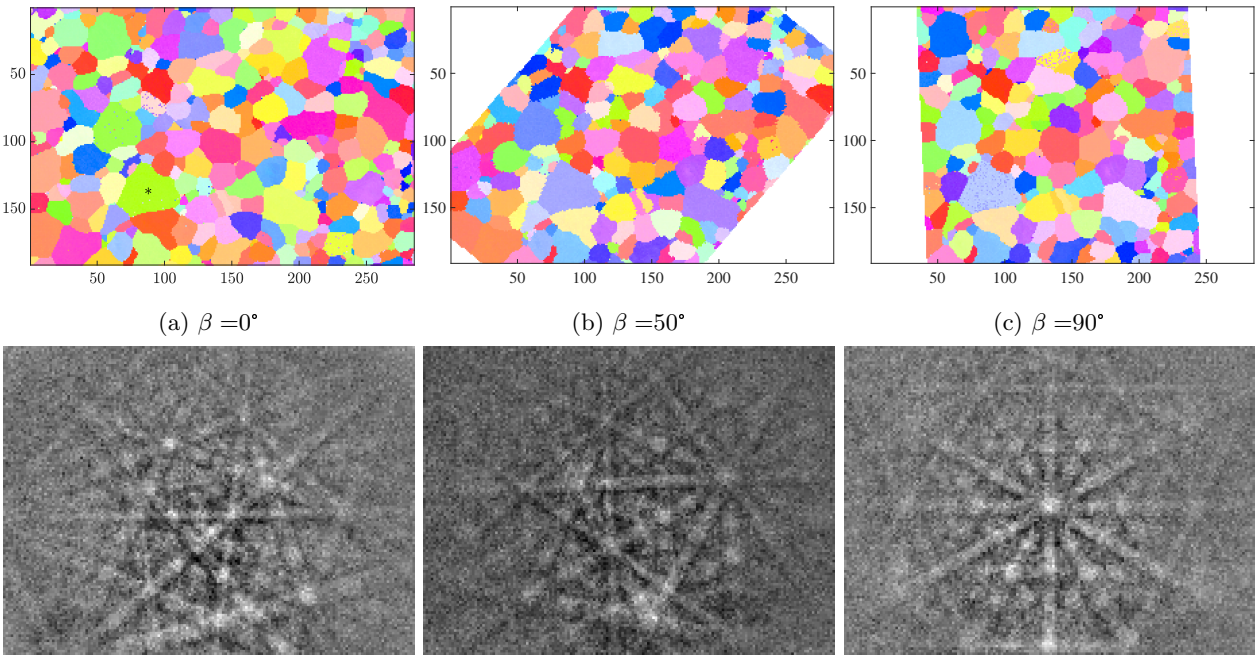

(a) β =0° (b) β =50° (c) β =90°

(d) (e) (f)

Figure 9: The inverse pole figure-Z of a fine grain Zircaloy-4, sample D, with different rotation angle β (a) 0°, (b) 50° and (c) 90°. The IPFs of (b) and (c) are transformed into the coordinates of (a). Three illustrations of EBSPs for the three acquisitions of the same grain marked by a star in (a) are shown in (d-f).

The measured misorientations by EBSD analysis are compared with the prescribed rotation due to different β. Based on the Hough indexation results, their distances are shown in Figure 10. Theoretically, the rotation caused by β can be represented by a unitary quaternion $[\cos(\beta/2), 0, 0, \sin(\beta/2)]$. Figures 10a-10b shows the misorientation deviation α_{mis} based on Hough indexation between $\beta = 0°$, 50° and $\beta = 0°$ and 90°, respectively. The average misorientation deviation with respect to $\beta = 0°$ increases from 2.1° to 2.7° when β passes from 50° to 90°. This is mainly due to the sample bad positioning (misalignment), which is more pronounced for large rotations. This misalignment can be evidenced by the skewness of figure 9c, which would be strictly vertical for a well-calibrated experiment.

Figures 10c-10e plot the Rodrigues' vector components $(\omega_X, \omega_Y, \omega_Z)$ between $\beta = 0,\ 90°$ for the Hough indexation results. ω_X and ω_Y are close to 0, while ω_Z have non-zero values. This conforms to expectation, as the sample rotation on the stage holder corresponds to the rotation component ω_Z. However, ω_Z is not uniform in Figure 10e, which is more pronounced in the linearly fitted fields shown in Figures 10f-10h. This global trend of ω_Z is due to the inaccurate EBSD calibrations in Hough indexation, which also explains the global trend in the α_{mis} shown in Figure 10b.

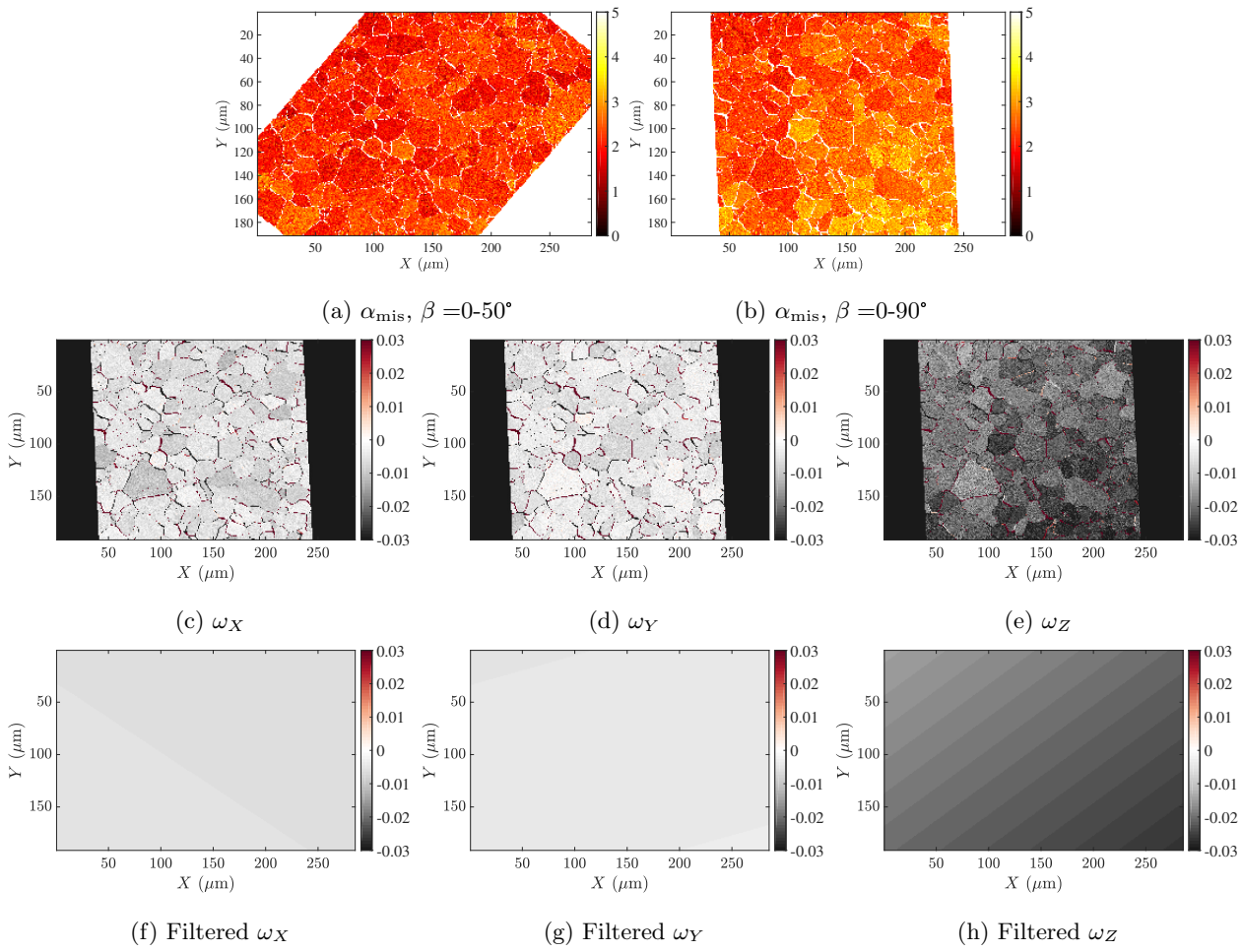

(a) α_{mis}, β =0-50° (b) α_{mis}, β =0-90°

(c) ω_X (d) ω_Y (e) ω_Z

(f) Filtered ω_X (g) Filtered ω_Y (h) Filtered ω_Z

Figure 10: The misorientation deviation analysis for Hough indexation based on the theoretical β relationships. (a) The misorientation deviation between β=0 and 50°; (b) The misorientation deviation between β=0 and 90°; (c-e) The Rodrigues' vector components between β=0 and 90°: (f-h) The linearly fitted Rodrigues' vector components between β=0 and 90°.

Their misorientation deviation results, based on the IDIC3 indexation results, are shown in Figure 11. Figures 11a–11b show the misorientation deviation α_{mis} based on IDIC3 indexation between $\beta = 0°$, 50° and $\beta =$ 0°, 90°, respectively. Figures 11c-11e show the Rodrigues' vector components for $\beta = 0, 90°$, while Figures 11f-11h plot their corresponding linear fitting results. Several remarks can be made:

- Similar to the Hough indexation results, the average misorientation deviation with respect to $\beta = 0°$ increases from 1.9° to 2.5° when β goes from 50° to 90°. This is due to the bad positioning of the sample, which deviates the true rotation from the theoretical one noted by the unitary quaternion $[\cos(\beta/2), 0, 0, \sin(\beta/2)]$.
- There are no global trends in Rodrigues' vector components. This phenomenon highlights the good calibration and indexation results of the IDIC EBSD algorithm. Although the actual rotation differs from the theoretical one, IDIC indexation can reveal the overall true rotations. This finding paves the way for orientation accuracy estimation by comparing it with the true rotation.

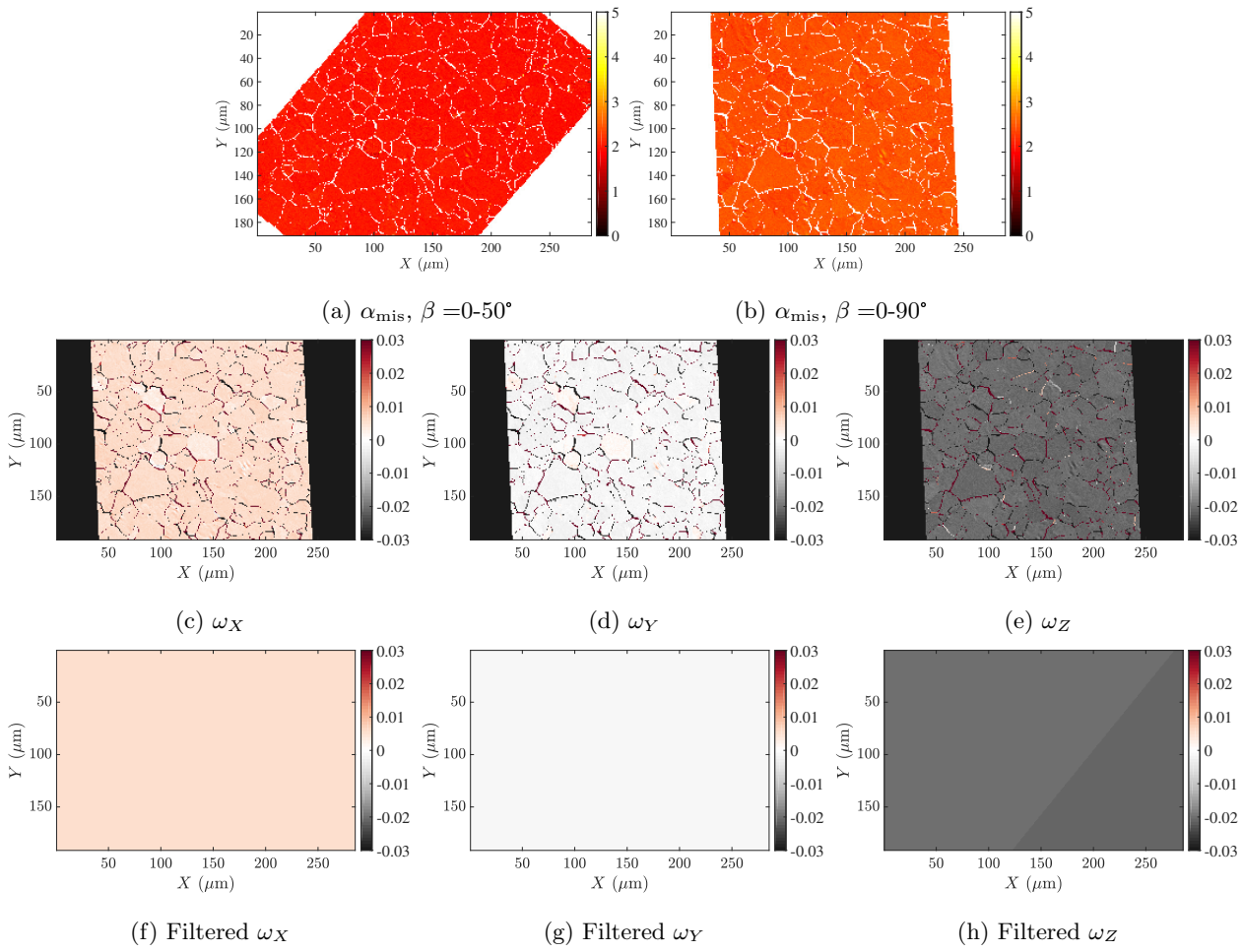

(a) α_{mis}, β =0-50˚ (b) α_{mis}, β =0-90˚

(c) ω_X (d) ω_Y (e) ω_Z

(f) Filtered ω_X (g) Filtered ω_Y (h) Filtered ω_Z

Figure 11: The misorientation deviation analysis for IDIC3 indexation based on the theoretical β relationships. (a) The misorientation deviation between β=0 and 50˚; (b) The misorientation deviation between β=0 and 90˚; (c-e) The Rodrigues' vector components between β=0 and 90˚; (f-h) The linearly fitted Rodrigues' vector components between β=0˚ and 90˚.

Both the values of α, β and the rotation axis have their own errors, but α, β and the axis are uniform for each EBSD acquisition. This property allows the estimation of orientation accuracy, especially for polycrystal samples. The misorientation between $\beta = 0$˚ and 50˚ (90˚) indexed by Hough and IDIC methods, after correcting the overall quaternion of miscalibration, are shown in Figure 12. Their histograms are provided in Figures 12c and 12f. The average indexation error, in the form of orientation consistency in the sample rotation, is 0.103˚ and 0.124˚ respectively for IDIC3 indexation of $\beta = 50, 90$˚, compared to 0.50˚ for Hough indexation. The crystal orientation error is roughly the same, except for a few grains.

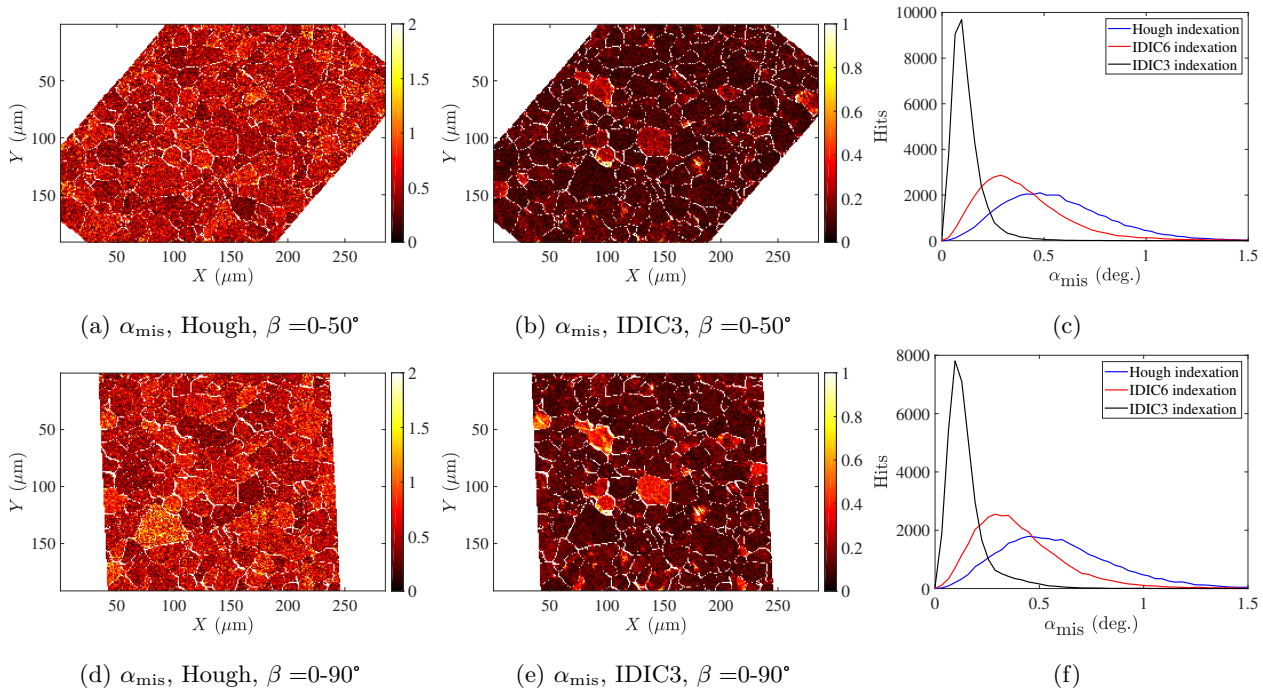

(a) α_{mis}, Hough, β =0-50° (b) α_{mis}, IDIC3, β =0-50° (c)

(d) α_{mis}, Hough, β =0-90° (e) α_{mis}, IDIC3, β =0-90° (f)

Figure 12: The misorientation deviation, after correcting the miscalibration quaternion, between rotation angle $\beta = 0°$ and 50°. (a) Hough indexation; (b) IDIC indexation; (c) plots the histogram comparison between (a) and (b); The same plots between $\beta = 0°$ and 90° are shown in (d-f).

Table 1: Summary of orientation accuracy for different algorithms and data sets

Sample	A (Ni)	B (Ni) [41]	C (Al-Mg) [24]			D (Zr) [47]	
Definition	228×320	60×60	1200×1600			120×160	
Rotation pair	FCC twin ⟨111⟩ 60°		θ=70°, 65° $\beta = 0°$	θ=70°, 60° $\beta = 0°$	θ=65°, 60° $\beta = 0°$	$\theta = 70°$ β=0°, 50°	$\theta = 70°$ β=0°, 90°
Hough (°)	0.858	1.03	0.739	1.10	0.677	0.529	0.555
DI (°)	0.995	1.24	–	–	–	–	–
Refined DI (°)	0.359	0.913	–	–	–	–	–
IDIC6 (°)	0.489	1.26	0.0523	0.119	0.120	0.355	0.367
IDIC3 (°)	0.344	**0.902**	**0.0376**	0.0745	0.0789	**0.103**	**0.124**
IDIC-G6 (°)	0.475	Not converge	0.0465	0.0829	0.0893	Not converge	Not converge
IDIC-G3 (°)	**0.338**	Not converge	0.0380	**0.0705**	**0.0767**	Not converge	Not converge

The estimated accuracy of IDIC, IDIC-G, dictionary indexing with or without refinement, and Hough indexation based on the two indicators is summarized in Table 1. Some cases are missing; for example, IDIC-G relies on high-frequency signals and does not converge on low-quality EBSPs such as dataset B&D. Besides, dictionary indexing is computation intensive, and it becomes prohibitively high when calculating high-resolution

patterns of dataset C. The indexation method with the largest error is marked red for each data set, and the lowest error is in bold font. Several conclusions could be drawn:

1. FPM methods lead to better accuracy as compared to Hough indexation. The improvement could be nearly 20-fold for high-quality EBSPs and down to 14% for fast acquisitions. FPM's more accurate crystal orientations would contribute to orientation-based characterization techniques, such as the GND density evaluation on each slip system [10].

2. The accuracy of the conventional Hough indexation lies in the interval of 0.5°– 1.0°. Moreover, the accuracy of Hough indexation does not improve for high-quality EBSPs. This observation is comparable to several previous studies [31, 34].

3. Remapping with a filtered PC field can refine crystal orientations, and this effect is more pronounced for IDIC. This is due to the PC deviation (discontinuity of PC at grain boundaries) of IDIC calibration being corrected in PC filtering. This PC fitting operation has less effect on IDIC-G, as it is less prone to systematic errors in PC calibration in the first place [24].

4. The accuracy estimation method by natural twins tends to overestimate the error level. This method relies on the EBSPs on the twin boundaries, where the pattern quality tends to decrease due to eventual strains and pattern overlaps. Besides, the assumption that the crystal orientation on one side of the boundary is exact makes this estimation an upper bound of the orientation error level, as the orientation errors of both sides of the twin are accumulated in the estimate. The accuracy level given by hardware rotations is a fair estimation. Nevertheless, the performance comparison of different indexation algorithms for each data set remains valuable.

5. For high-quality EBSPs, IDIC-G leads to better orientation accuracy up to 0.038°. For very low-quality EBSPs, IDIC has an error level around 0.9°, an overestimated value as explained previously.

5 Conclusion

There is a long-lasting quest for crystal orientation accuracy estimation, for which the primary difficulty is the unknown ground truth of the orientations. This paper provides two estimation methods based on natural and hardware orientation relationships to circumvent the obstacle. The present work extensively tests both methods on different experimental EBSP data sets.

1. Exploitation of complete orientation relationships (OR) in the sample, especially twinning. The current work takes the example of Ni twins and proposes to consider both the theoretical rotation axis ($\langle 111 \rangle$) and theoretical rotation angle (60°) in the accuracy evaluation. If the analysis does not include the rotation axis, measurement error will be underestimated. This method is easy to use and needs only one data acquisition, yet requires the existence of special ORs.

2. Application of a physical rotation of the sample between multiple data acquisitions and comparison of the retrieved crystal orientation rotation with the imposed one. The rotation angle and the axis of the physical rotation are used again in the comparison. This method has no requirement on the sample but

necessitates multiple acquisitions. Besides, when the indexation method has an optimal positioning, such as the 70° tilt for EBSD, the accuracy will be affected by this sample rotation.

The two accuracy estimation methods apply to the EBSD technique and other indexation methods, such as TKD, TEM-based, chemical etch-based, or optical reflectance methods.

The paper also demonstrates that the full pattern matching method, represented by IDIC EBSD calibration and dictionary indexing with refinement, provides better accuracy and precision than other crystal orientation indexation methods, such as Hough indexations. The improvement of orientation indexation compared to Hough indexation could be nearly 20-fold for high-quality EBSPs, and down to 14% for fast acquisitions.

Acknowledgements

This work is financially supported by the National Key Research and Development Program of China, 2021YFA1600900, and the National Natural Science Foundation of China [No. 52273229, 51901132, 52204393]. We are also grateful for the financing from TESCAN CHINA, Ltd and EDF.

Data Availability

The high-quality diffraction patterns of the polycrystal Al-Mg alloy of different sample tilt angles are available at Zenodo (DOI: 10.5281/zenodo.7528088 and 10.5281/zenodo.6990325). The Ni EBSD data set of medium quality is available at Zenodo (DOI: 10.5281/zenodo.7937129), while the Ni EBSD data set of fast acquisition was shared by Jackson *et al.* [41]. The Zircalloy EBSD data sets of different sample positioning are shared by Birch & Britton at Zenodo (DOI: https://doi.org/10.5281/zenodo.4925663). The indexation results for all these data are also provided, including the crystal orientations and calibrated PC coordinates, with the full pattern or its gradient norms, with the floating PC coordinates or the filtered ones. We invite interested colleagues to use these data sets to improve the accuracy of EBSD indexation further.

References

[1] S.I. Wright and B.L. Adams. Automatic analysis of electron backscatter diffraction patterns. *Metallurgical Transactions A*, 23(3):759–767, 1992.

[2] C. Maurice and R. Fortunier. A 3D Hough transform for indexing EBSD and Kossel patterns. *Journal of Microscopy*, 230(3):520–529, 2008.

[3] Y.H. Chen, S.U. Park, D. Wei, G. Newstadt, M.A. Jackson, J.P. Simmons, M. De Graef, and A.O. Hero. A dictionary approach to electron backscatter diffraction indexing. *Microscopy and Microanalysis*, 21(3):739–752, 2015.

[4] F. Ram, S. Wright, S. Singh, and M. De Graef. Error analysis of the crystal orientations obtained by the dictionary approach to EBSD indexing. *Ultramicroscopy*, 181(Supplement C):17 – 26, 2017.

[5] W.C. Lenthe, S. Singh, and M. De Graef. A spherical harmonic transform approach to the indexing of electron back-scattered diffraction patterns. *Ultramicroscopy*, 207:112841, 2019.

[6] D. Jha, S. Singh, R. Al-Bahrani, W. Liao, A. Choudhary, M. De Graef, and A. Agrawal. Extracting grain orientations from EBSD patterns of polycrystalline materials using convolutional neural networks. *Microscopy and Microanalysis*, 24(5):497–502, 2018.

[7] Z. Ding, E. Pascal, and M. De Graef. Indexing of electron back-scatter diffraction patterns using a convolutional neural network. *Acta Materialia*, 199:370 – 382, 2020.

[8] F. Ram and M. De Graef. Phase differentiation by electron backscatter diffraction using the dictionary indexing approach. *Acta Materialia*, 144:352 – 364, 2018.

[9] A. Seret, C. Moussa, M. Bernacki, J. Signorelli, and N. Bozzolo. Estimation of geometrically necessary dislocation density from filtered EBSD data by a local linear adaptation of smoothing splines. *Journal of Applied Crystallography*, 52(3):548–563, 2019.

[10] E. Demir, E. Horton, A. Kareer, D. Collins, M. Mostafavi, and D. Knowles. A finite element method to calculate geometrically necessary dislocation density: Accounting for orientation discontinuities in polycrystals. *Acta Materialia*, 245:118658, 2023.

[11] S. Singh, F. Ram, and M. DeGraef. Application of forward models to crystal orientation refinement. *Journal of Applied Crystallography*, 50, 2017.

[12] T. Friedrich, A. Bochmann, J. Dinger, and S. Teichert. Application of the pattern matching approach for EBSD calibration and orientation mapping, utilising dynamical EBSP simulations. *Ultramicroscopy*, 184:44 – 51, 2018.

[13] T. Tanaka and A.J. Wilkinson. Pattern matching analysis of electron backscatter diffraction patterns for pattern centre, crystal orientation and absolute elastic strain determination - accuracy and precision assessment. *Ultramicroscopy*, 202:87–99, 2019.

[14] A. Winkelmann, G. Nolze, G. Cios, T.Tokarski, and P. Bała. Refined calibration model for improving the orientation precision of electron backscatter diffraction maps. *Materials*, 13:2816, 2020.

[15] A. Winkelmann, B. Jablon, V. Tong, C. Trager-Cowan, and K. Mingard. Improving EBSD precision by orientation refinement with full pattern matching. *Journal of Microscopy*, 277(2):79–92, 2020.

[16] E.L. Pang, P.M. Larsen, and C.A. Schuh. Global optimization for accurate determination of EBSD pattern centers. *Ultramicroscopy*, 209:112876, 2020.

[17] C. Zhu, C. Kurniawan, M. Ochsendorf, D. An, S. Zaefferer, and M. De Graef. Orientation, pattern center refinement and deformation state extraction through global optimization algorithms. *Ultramicroscopy*, 233:113407, 2022.

[18] S. Singh, F. Ram, and M. De Graef. EMsoft: Open source software for electron diffraction/image simulations. *Microscopy and MicroAnalysis*, 23:S1:212–213, 2017.

[19] T. Vermeij, M. De Graef, and J. Hoefnagels. Demonstrating the potential of accurate absolute cross-grain stress and orientation correlation using electron backscatter diffraction. *Scripta Materialia*, 162:266 – 271, 2019.

[20] B. Pan, H. Xie, and Z. Wang. Equivalence of digital image correlation criteria for pattern matching. *Applied Optics*, pages 5501–5509, 2010.

[21] Q. Shi, D. Loisnard, C. Dan, F. Zhang, H. Zhong, H. Li, Y. Li, Z. Chen, H. Wang, and S. Roux. Calibration of crystal orientation and pattern center of EBSD using integrated digital image correlation. *Materials Characterization*, 178:111206, 2021.

[22] Q. Shi, Y. Zhou, H. Zhong, D. Loisnard, C. Dan, F. Zhang, Z. Chen, H. Wang, and S. Roux. Indexation of electron diffraction patterns at grain boundaries. *Materials Characterization*, 182:111553, 2021.

[23] Q. Shi, L. Jiao, D. Loisnard, C. Dan, Z. Chen, H. Wang, and S. Roux. Improved EBSD indexation accuracy by considering energy distribution of diffraction patterns. *Materials Characterization*, 188:111909, 2022.

[24] Q. Shi, H. Zhong, D. Loisnard, L. Wang, Z. Chen, H. Wang, and S. Roux. Enhanced EBSD calibration accuracy based on gradients of diffraction patterns. *Materials Characterization*, 202:113022, 2023.

[25] G. Nolze, A. Winkelmann, G. Cios, and T. Tokarski. Tetragonality mapping of martensite in a high-carbon steel by EBSD. *Materials Characterization*, 175:111040, 2021.

[26] D. Adams, M. Miles, E. Homer, T. Brown, R. Mishra, and D. Fullwood. Phase determination in dual phase steels via HREBSD-based tetragonality mapping. *Journal of Microscopy*, 282(1):60–72, 2021.

[27] A.J. Wilkinson, G. Meaden, and D.J. Dingley. High-resolution elastic strain measurement from electron backscatter diffraction patterns: New levels of sensitivity. *Ultramicroscopy*, 106(4-5):307 – 313, 2006.

[28] A. Koko, E. Elmukashfi, K. Dragnevski, A. Wilkinson, and T. Marrow. J-integral analysis of the elastic strain fields of ferrite deformation twins using electron backscatter diffraction. *Acta Materialia*, 218:117203, 2021.

[29] G. Nolze, T. Tokarski, and Ł. Rychłowski. Use of electron backscatter diffraction patterns to determine the crystal lattice. Part 1. Where is the Bragg angle? *Journal of Applied Crystallography*, 56(2), 2023.

[30] Researchgate. How precise an orientation determination by EBSD under typical conditions can be?, 2014. https://www.researchgate.net/post/How-precise-an-orientation-determination-by-EBSD-under-typical-conditions-can-be Accessed: 2023-08-01.

[31] J. Venables and R. Bin-jaya. Accurate microcrystallography using electron back-scattering patterns. *Philosophical Magazine*, 35(5):1317–1332, 1977.

[32] N. Lassen. The relative precision of crystal orientations measured from electron backscattering patterns. *Journal of Microscopy*, 181:72 – 81, 1996.

[33] D.J. Prior. Problems in determining the misorientation axes, for small angular misorientations, using electron backscatter diffraction in the sem. *Journal of Microscopy*, 195(3):217–225, 1999.

[34] M. Demirel, B. El-Dasher, B. Adams, and A. Rollett. *Studies on the Accuracy of Electron Backscatter Diffraction Measurements*, pages 65–74. Springer US, 2000.

[35] S. Wright, J. Basinger, and M. Nowell. Angular precision of automated electron backscatter diffraction measurements. *Materials Science Forum*, 702-703:548–553, 2012.

[36] F. Ram, S. Zaefferer, T. Jäpel, and D. Raabe. Error analysis of the crystal orientations and disorientations obtained by the classical electron backscatter diffraction technique. *Journal of Applied Crystallography*, 48(3):797–813, 2015.

[37] S. I. Wright and R. J. Larsen. Extracting twins from orientation imaging microscopy scan data. *Journal of Microscopy*, 205(3):245–252, 2002.

[38] Y. Shen, Y. Zhang, W. Li, H. Miao, Y. Wang, and Y. Zeng. Local kikuchi band detection in electron backscatter diffraction patterns for enhanced pattern indexing. *Journal of Microscopy*, 284(3):256–265, 2021.

[39] F. Peng, Y. Zhang, W. Li, H. Miao, and Y. Zeng. A New Method for Evaluating the Accuracy of the Orientation Measured by Different Kikuchi Pole Combinations in Kikuchi Patterns. *Microscopy and Microanalysis*, 29(1):202–211, 2023.

[40] G. Nolze, M. Jürgens, J. Olbricht, and A. Winkelmann. Improving the precision of orientation measurements from technical materials via EBSD pattern matching. *Acta Materialia*, 159:408 – 415, 2018.

[41] M. Jackson, E. Pascal, and M. Graef. Dictionary indexing of electron back-scatter diffraction patterns: a hands-on tutorial. *Integrating Materials and Manufacturing Innovation*, 8:226–246, 2019.

[42] A. Wilkinson. A new method for determining small misorientations from electron back scatter diffraction patterns. *Scripta materialia*, 44(10):2379–2385, 2001.

[43] Q. Shi, F. Latourte, F. Hild, and S. Roux. Quaternion correlation for tracking crystal motions. *Measurement Science and Technology*, 27(9):095006, 2016.

[44] M. Kamaya, A. Wilkinson, and J. Titchmarsh. Quantification of plastic strain of stainless steel and nickel alloy by electron backscatter diffraction. *Acta materialia*, 54(2):539–548, 2006.

[45] S.I. Wright, M. Nowell, S.P. Lindeman, P. Camus, M. De Graef, and M.A. Jackson. Introduction and comparison of new EBSD post-processing methodologies. *Ultramicroscopy*, 159, Part 1:81 – 94, 2015.

[46] A. Winkelmann and G. Nolze. Analysis of kikuchi band contrast reversal in electron backscatter diffraction patterns of silicon. *Ultramicroscopy*, 110:190–194, 2010.

[47] R. Birch and B. Britton. Dataset: Zr EBSD maps rotated at 0, 50 & 90 degrees, June 2021. Zenodo.

[48] Q. Shi, S. Roux, F. Latourte, F. Hild, D. Loisnard, and N. Brynaert. On the use of SEM correlative tools for in situ mechanical tests. *Ultramicroscopy*, 184(Part A):71 – 87, 2018.